

# Atmospheric characterization and tighter constraints on the orbital misalignment of WASP-94 A b with HARPS

E. Ahrer<sup>ID, 1,2,3,4\*</sup> J. V. Seidel<sup>ID, 5†</sup> L. Doyle,<sup>1,2</sup> S. Gandhi<sup>ID, 1,2,6</sup> B. Prinoth,<sup>5,7</sup> H. M. Cegla<sup>ID, 1,2,†</sup>  
C. H. McDonald<sup>ID, 1,2,8</sup> N. Astudillo-Defru<sup>ID, 9</sup> E. Ayache<sup>ID, 10</sup> R. Nealon<sup>ID, 1,2</sup> Dimitri Veras<sup>ID, 1,2,11</sup>  
P. J. Wheatley<sup>ID, 1,2</sup> and D. Ehrenreich<sup>12</sup>

<sup>1</sup>Centre for Exoplanets and Habitability, University of Warwick, Gibbet Hill Road, CV4 7AL Coventry, UK

<sup>2</sup>Department of Physics, University of Warwick, Gibbet Hill Road, CV4 7AL Coventry, UK

<sup>3</sup>Department of Physics and Astronomy, Faculty of Environment, Science and Economy, University of Exeter, Exeter EX4 4QL, UK

<sup>4</sup>Max Planck Institute for Astronomy (MPIA), Königstuhl 17, D-69117 Heidelberg, Germany

<sup>5</sup>European Southern Observatory, Alonso de Córdova 3107, Vitacura, Región Metropolitana, Chile

<sup>6</sup>Leiden Observatory, Leiden University, Postbus 9513, NL-2300 RA Leiden, The Netherlands

<sup>7</sup>Lund Observatory, Division of Astrophysics, Department of Physics, Lund University, Box 43, SE-221 00 Lund, Sweden

<sup>8</sup>Institute of Astronomy, University of Cambridge, Madingley Road, Cambridge, CB3 0HA, UK

<sup>9</sup>Departamento de Matemática y Física Aplicadas, Universidad Católica de la Santísima Concepción, Alonso de Rivera 2850, Concepción, Chile

<sup>10</sup>The Oskar Klein Centre, Department of Astronomy, Stockholm University, AlbaNova, SE-106 91 Stockholm, Sweden

<sup>11</sup>Centre for Space Domain Awareness, University of Warwick, Gibbet Hill Road, CV4 7AL Coventry, UK

<sup>12</sup>Observatoire astronomique de l'Université de Genève, Chemin Pegasi 51b, CH-1290 Versoix, Switzerland

Accepted 2024 April 6. Received 2024 April 4; in original form 2024 January 31

## ABSTRACT

We present high spectral resolution observations of the hot Jupiter WASP-94 A b using the HARPS instrument on ESO's 3.6-m telescope in La Silla, Chile. We probed for Na absorption in its atmosphere as well as constrained the previously reported misaligned retrograde orbit using the Rossiter–McLaughlin effect. Additionally, we undertook a combined atmospheric retrieval analysis with previously published low-resolution data. We confirm the retrograde orbit as well as constrain the orbital misalignment with our measurement of a projected spin-orbit obliquity of  $\lambda = 123.0 \pm 3.0^\circ$ . We find a tentative detection of Na absorption in the atmosphere of WASP-94 A b, independent of the treatment of the Rossiter–McLaughlin effect in our analysis ( $3.6\sigma$  and  $4.4\sigma$ ). We combine our HARPS high-resolution data with low-resolution data from the literature and find that while the posterior distribution of the Na abundance results in a tighter constraint than using a single data set, the detection significance does not improve ( $3.2\sigma$ ), which we attribute to degeneracies between the low- and high-resolution data.

**Key words:** methods: observational – techniques: spectroscopic – exoplanets – planets and satellites: atmospheres – planets and satellites: individual: WASP-94 A b.

## 1 INTRODUCTION

Hot Jupiters – Jupiter-sized exoplanets orbiting their host stars at a close distance – have been at the forefront of exoplanet research as they exhibit relatively large signatures when observing both transit events and obtaining radial velocity measurements due to their closeness to the host star and large size and mass (e.g. Mayor & Queloz 1995; Charbonneau et al. 2000). In addition, they can also show extended atmospheres that result in large atmospheric signatures that can be detected, e.g. using transmission spectroscopy (e.g. Charbonneau et al. 2002; Snellen et al. 2008, 2010; Pont et al. 2013; Sing et al. 2016). Due to their large temperatures hot and ultra-

hot Jupiters have dissociated atmospheres, i.e. elements such as Na exist in their atomic and ionic form (e.g. Seager & Sasselov 2000).

Transmission spectroscopy is the method of determining transit depth versus wavelength and is used to study the atmospheres of exoplanets, identifying molecules and atomic species as well as clouds and hazes that absorb the transmitted light in the observed wavelength ranges. It has been successfully applied in low-spectral resolution as well as high-spectral resolution regimes. While low resolution spectroscopy allows for studying broad-band features e.g. scattering slopes and clouds (e.g. Lecavelier Des Etangs et al. 2008; Kreidberg et al. 2014; Sing et al. 2015; Kirk et al. 2017; Espinoza et al. 2019; Spyros et al. 2021; Ahrer et al. 2023a) as well as atomic and molecular signatures such as Na (e.g. Charbonneau et al. 2002; Redfield et al. 2008; Nikolov et al. 2018; Alderson et al. 2020), water vapour (e.g. Huitson et al. 2013; Wakeford & Sing 2015; Kreidberg et al. 2018; Carone et al. 2021; Feinstein et al. 2023; Ahrer et al. 2023c), carbon dioxide (e.g. Taylor et al. 2023; The JWST Transiting Exoplanet Community Early Release Science Team et al. 2023) and

\* E-mail: [ahrer@mpia.de](mailto:ahrer@mpia.de) (EA); [jseidel@eso.org](mailto:jseidel@eso.org) (JVS)

† ESO Fellow

‡ UKRI Future Leaders Fellow

**Table 1.** Stellar and planetary parameters for the WASP-94 A planetary system. References are as follows: [1] Neveu-Vanmalle et al. (2014), [2] Teske, Khanal & Ramírez (2016), [3] Bonomo et al. (2017), [4] Gaia Collaboration et al. (*Gaia* DR3, 2023), [5] Andrae et al. (*Gaia* DR3 GSP-Phot, 2023), and [6] Garhart et al. (2020).

Stellar parameters of WASP-94 A		
Parameter	WASP-94 A	Reference
Brightness, $V_{\text{mag}}$	10.1	[1]
Spectral type	F8	[1]
Effective Temperature, $T_{\text{eff}}$ (K)	$6194 \pm 5$	[2]
Age (Gyr)	$2.55 \pm 0.25$	[2]
Surface gravity, $\log g$ ( $\log_{10}(\text{cm s}^{-2})$ )	$4.210 \pm 0.011$	[2]
Metallicity [Fe/H]	$0.320 \pm 0.004$	[2]
Mass, $M_*$ ( $M_{\odot}$ )	$1.450 \pm 0.090$	[3], [1]
Radius, $R_*$ ( $R_{\odot}$ )	$1.5784^{+0.0095}_{-0.0110}$	[4,5]
Systemic velocity $\gamma$ ( $\text{km s}^{-1}$ )	$8.36 \pm 0.19$	[5]
Planetary parameters of WASP-94 A b		
Parameter	Value	Reference
Period, P (d)	$3.9501907^{+0.0000044}_{-0.000030}$	[1]
Semimajor axis, $a$ (au)	$0.0554^{+0.0012}_{-0.0011}$	[3]
Mass, $M_p$ ( $M_{\text{Jup}}$ )	$0.456^{+0.034}_{-0.036}$	[3]
Radius, $R_p$ ( $R_{\text{Jup}}$ )	$1.72^{+0.06}_{-0.05}$	[1]
Inclination, $i$ ( $^{\circ}$ )	$88.7 \pm 0.7$	[1]
Surface gravity, $\log g$ ( $\log_{10}(\text{cm s}^{-2})$ )	$2.590^{+0.044}_{-0.042}$	[3]
Equilibrium temperature, $T_{\text{eq}}$ (K)	$1508 \pm 75$	[6]

sulphur dioxide bands (Alderson et al. 2023; Dyrek et al. 2024; Rustamkulov et al. 2023), high resolution spectroscopy is used to identify species by resolving their individual lines e.g. Fe/Fe + (e.g. Hoeijmakers et al. 2018, 2019; Ehrenreich et al. 2020; Gandhi et al. 2022), Na doublet (e.g. Casasayas-Barris et al. 2018; Seidel et al. 2019; Hoeijmakers et al. 2020; Prinot et al. 2022), He (e.g. Salz et al. 2018; Spake et al. 2018; Allart et al. 2019), among many others.

Combining low- and high-resolution transmission spectroscopy observations allows us to probe for both individual lines as well as continuum in exoplanetary atmospheres (e.g. Brogi et al. 2017; Pino et al. 2018; Khalafinejad et al. 2021). For example, Brogi et al. (2017) showed that combining low resolution data from Hubble Wide Field Camera 3 (WFC3) and high-resolution observations with CRyogenic Infra-Red Echelle Spectrograph (CRIRES) can result in much tighter retrieved constraints on atmospheric abundances in an exoplanet atmosphere, in this case the hot Jupiter HD 209458 b.

In this work, we present high-resolution transit observations of WASP-94 A b using the HARPS instrument (High Accuracy Radial Velocity Planet Searcher; Mayor et al. 2003) at ESO's 3.6-m telescope at La Silla, Chile. HARPS has been utilized to detect exoplanets (e.g. Udry et al. 2007; Bonfils et al. 2013; Delisle et al. 2018; Unger et al. 2021) as well as for the characterization of exoplanet atmospheres (e.g. Wyttenbach et al. 2017; Seidel et al. 2019; Mounzer et al. 2022; Steiner et al. 2023).

WASP-94 A b is a hot Jupiter with a mass of half of Jupiter's and a radius of  $1.72 R_{\text{Jup}}$  (see Table 1). We further introduce the WASP-94 system in Section 2, followed by a summary of the HARPS observations in Section 3. We show the Rossiter–McLaughlin effect analysis in Section 4, which includes the updated constraint on the orbital alignment. Our analysis of WASP-94 A b's atmosphere in the form of a transmission spectrum and atmospheric retrieval

is presented in Sections 5 and 6. We conclude the paper in Section 7.

## 2 WASP-94 SYSTEM

The WASP-94 system consists of two F-type stars, WASP-94 A (F8) and WASP-94 B (F9) with V magnitudes of 10.1 and 10.5, respectively. Their angular distance is  $15.03 \pm 0.01$  arcsec and their orbital separation is estimated to be at 2700 AU (Neveu-Vanmalle et al. 2014). Using *Gaia* DR2, the distance of the system was determined to be  $212.46 \pm 2.50$  pc (*Gaia* DR2, Bailer-Jones et al. 2018).

Neveu-Vanmalle et al. (2014) discovered that both stars host a planetary satellite: WASP-94 A b is transiting and seen in RV measurements while WASP-94 B b does not transit and has been detected by RV measurements only. WASP-94 A b is a hot Jupiter, with a radius of  $1.72^{+0.06}_{-0.05} R_{\text{Jup}}$  (Neveu-Vanmalle et al. 2014), a mass of  $0.456^{+0.034}_{-0.036} M_{\text{Jup}}$  (Bonomo et al. 2017) and an equilibrium temperature of  $1508 \pm 75$  K (Garhart et al. 2020), orbiting its host star in a  $3.9501907^{+0.0000044}_{-0.000030}$  d period (Neveu-Vanmalle et al. 2014). WASP-94 B b is a Jupiter-sized planet with an orbital period of  $2.00839 \pm 0.00024$  d (Neveu-Vanmalle et al. 2014). All relevant stellar and planetary parameters of the WASP-94 A system are summarized in Table 1. Note that for our modelling of the planetary transit and Rossiter–McLaughlin correction, we did not use the planet radius and stellar radius separately as displayed in Table 1, instead we used the ratio of planet to star radius  $R_p/R_* = 0.10859$  in the Na wavelength range from Ahrer et al. (2022).

By measuring the Rossiter–McLaughlin (RM) effect (McLaughlin 1924; Rossiter 1924) using observations with the CORALIE instrument (Baranne et al. 1996), Neveu-Vanmalle et al. (2014) found that the orbit of WASP-94 A b is misaligned and likely retrograde with a spin-orbit obliquity of  $\lambda = 151^{\circ} \pm 20^{\circ}$ .

WASP-94 A b's atmosphere has been previously studied with the EFOSC2 spectrograph on the New Technology Telescope (NTT). Ahrer et al. (2022) presented a low resolution transmission spectrum from 4020–7140 Å, showing evidence for a scattering slope as well as a Na absorption feature.

## 3 OBSERVATIONS

Observations of WASP-94 A took place as part of the HEARTS survey (ESO programme 097.C-1025(B); PI: Ehrenreich). We collected data of one transit of WASP-94 A b on the night of 2016 July 15 using the HARPS spectrograph (Mayor et al. 2003). The weather conditions were adequate, slightly affected by thin clouds. The humidity ranged from 30 per cent at the beginning of the night up to 70 per cent around midnight and down to 40 per cent at the end of the night. The seeing was not recorded.

Overall 55 exposures were taken: 5 before the transit, 26 during the transit, and 24 after the transit. The airmass values ranged from 2.44 at the beginning of the night, down to 1.004 during the maximum altitude and up to 1.75 at the end of the night. The signal-to-noise (SNR) at the wavelength range of the Na doublet varied throughout the night from 26 up to 62, with a median value of 48. The exposure times for all frames were 600s, except for the first one, which was exposed for 700s.

The HARPS Data Reduction Pipeline (DRS v3.8) extracts the spectra order by order from the 2D images from the Echelle spectrograph and are stored as e2ds.fits files. The region of the Na doublet lies in the order number 56, covering a wavelength range of 5850.24 to 5916.17 Å.

#### 4 ROSSITER–MCLAUGHLIN ANALYSIS

When a planet transits a host star, a portion of the starlight is blocked from the line of sight and a distortion of the velocities is observed, known as the RM effect (see McLaughlin (1924); Rossiter (1924) for original studies and Queloz et al. (2000) for the first exoplanet case). The shape of the RM curve contains information about the planet-to-stellar radius ratio, the rotational velocity of the star, the impact parameter, and the projected obliquity,  $\lambda$ , which is the sky-projected angle between the stellar spin axis and planetary orbital plane. Neveu-Vanmalle et al. (2014) observed WASP-94 A b using the CORALIE spectrograph (Baranne et al. 1996) obtaining 24 measurements in transit and an additional 24 out-of-transit spectra over the full orbit. Through these observations, they found WASP-94 A b is misaligned and likely retrograde with a projected obliquity of  $\lambda = 151 \pm 20^\circ$ . In this study, we conduct our own analysis of the RM effect using the CORALIE measurements from Neveu-Vanmalle et al. (2014) in combination with our HARPS observations to further constrain the spin-orbit obliquity  $\lambda$ .

We utilized the reloaded-RM technique (RRM: Cegla et al. 2016), which isolates the blocked starlight behind the planet to spatially resolve the stellar spectrum and can be used to derive  $\lambda$ . First, the CORALIE and HARPS disc-integrated cross-correlation functions (CCFs) are shifted and re-binned in velocity space to correct for the Keplerian motions of the star induced by WASP-94 A b (using the orbital properties in Table 1). Next, for each observation, a master-out disc-integrated CCF was created through a summation of all out-of-transit disc-integrated CCFs followed by normalizing the continuum to unity. Each master-out disc-integrated CCF was then fitted by a Gaussian profile to determine the systemic velocity,  $\gamma$ , where this was subtracted from all disc-integrated CCFs to shift them to the stellar rest frame. Each disc-integrated CCF was normalized using the continuum and then scaled using a transit light curve model with quadratic limb darkening from the fitted transit parameters in Table 1. This allows the local CCFs to be obtained by directly subtracting in-transit disc-integrated CCFs from the master-out disc-integrated CCF for each night, see Fig. 1.

To determine the stellar velocity behind the occulted planet, we fit Gaussian profiles to each of the local CCFs, which included the parameters offset (i.e. continuum), amplitude, centroid, and FWHM. Flux errors were determined as the standard deviation of the continuum and were assigned to each local CCF and included in the Gaussian fit. The resulting local RVs of the planet's occulted starlight can be seen in Fig. 2 as a function of phase and stellar disc position behind the planet in units of brightness weighted  $\langle \mu \rangle$  (where  $\mu = \cos \theta$ ). We removed CCFs with limb angles  $\langle \mu \rangle < 0.30$  from our analysis, resulting in two CCFs being removed from the CORALIE observations. Close to the limb, local CCF profiles can be very noisy (see Cegla et al. 2016), in this case, the depth of the local CCF was not significant enough to enable a Gaussian fit; see Fig. 1, where they are shown as dashed lines.

The local RVs in Fig. 2 were fitted modelling the local, projected stellar velocities behind the planet described in Cegla et al. (2016), henceforth referred to as the RRM model. The model depends on the position of the transiting planet centre with respect to the stellar disc, projected obliquity ( $\lambda$ ), stellar inclination ( $i_*$ ), the equatorial rotational velocity ( $v_{\text{eq}}$ ), the differential rotational shear ( $\alpha$ ), quadratic stellar limb darkening ( $u_1$  and  $u_2$ ), and centre-to-limb convective variations (CLVs) of the star ( $v_{\text{conv}}$ ). For WASP-94 A, we fitted for different scenarios depending on whether or not we account for differential rotation (DR) and CLVs. We sample the RRM model parameters using a Markov Chain Monte Carlo (MCMC)

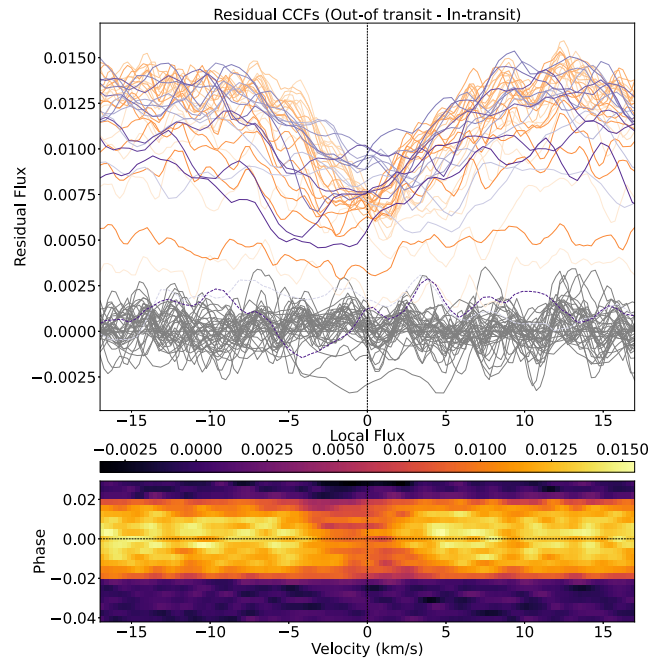


**Figure 1.** Top panel: The local CCFs (out-of-transit – in-transit) in the stellar rest frame of the star behind WASP-94 A b. The light grey lines are the out-of-transit observations, and the purple (CORALIE) and orange (HARPS) lines are the in-transit observations. The changing gradient of the orange/purple lines represents the changing centroid position, where the darker orange/purple is more redshifted. Dashed orange/purple lines are observations that have a stellar disc position  $\langle \mu \rangle < 0.30$  and are not used in the analysis. Bottom panel: A top view of all data from both CORALIE and HARPS showing a map of the local CCFs colour-coded by the local flux. A dotted line at phase zero and  $0 \text{ km s}^{-1}$  in both plots is included to guide the eye.

method implemented using the Python package emcee (Foreman-Mackey et al. 2013). A total of 200 walkers with 5000 steps and an additional burn-in phase of 5000 steps were used. For the solid body (SB) scenario, uniform priors were set on the RRM model parameters  $v_{\text{eq}} \sin i_* \sim \mathcal{U}(0, 100) \text{ km s}^{-1}$  and  $\lambda \sim \mathcal{U}(-180^\circ, 180^\circ)$ . When including DR, uniform parameters were included for  $\alpha \sim \mathcal{U}(-1.0, 1.0)$ ,  $i_* \sim \mathcal{U}(0^\circ, 180^\circ)$ ,  $v_{\text{eq}} \sim \mathcal{U}(0, 100) \text{ km s}^{-1}$  and  $\lambda \sim \mathcal{U}(-180^\circ, 180^\circ)$ . Finally, we initiate the walkers in a Gaussian ball around the maximum likelihood result. The results are summarized in Table 2 along with the Bayesian Information Criterion (BIC) for each of the models, where a lower value represents a better fit. Note that for all models using SB stellar rotation models  $i_*$  and  $\alpha$  are fixed under the assumption of rigid body rotation and the  $v_{\text{eq}}$  column corresponds to  $v_{\text{eq}} \sin i_*$ . For these models, we are unable to determine the 3D obliquity,  $\psi$ .

As WASP-94 A is an F8-type star with an effective temperature of  $T_{\text{eff}} = 6194 \text{ K}$ , we would expect to observe the net convective velocity shift caused by granules to change as a function of limb angle (i.e. from the centre to the limb of the star) due to line-of-sight changes. To account for this, we fit the local RVs for CLV and SB rotation at the same time adding a linear, quadratic, or cubic polynomial to the SB model fit as a function of limb angle. However, according to the BIC of the models, none of these are significant enough to be considered a detection of CLV. It is highly likely the signal to noise of the exposures in both the HARPS and CORALIE data is not high enough to allow for a clear detection (see Doyle et al. 2022, for an example with ESPRESSO of a similar spectral type). Finally, we fit

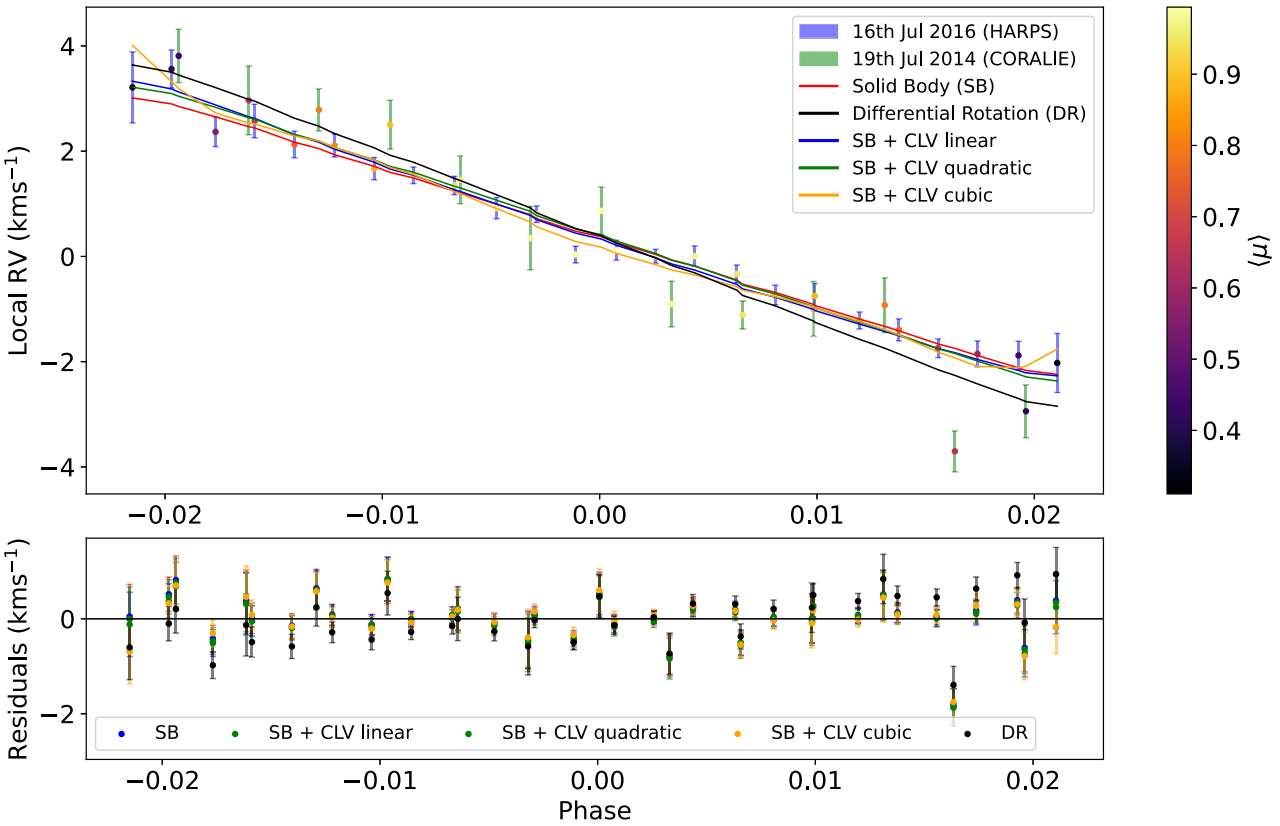


**Figure 2.** *Top panel:* The local RVs determined from the local CCFs of the regions occulted by the planet as a function of phase. The data points are colour coded by the stellar disc position behind the planet in units of brightness weighted  $\langle \mu \rangle$  (where  $\mu = \cos \theta$ ). The best-fit model for solid body rotation (SB: red line) is shown, along with the SB plus centre-to-limb linear (blue), SB plus centre-to-limb quadratic (green), SB plus centre-to-limb cubic (orange), and differential rotation (DR: black) models. *Bottom panel:* The residuals (local RVs – model) for all models with colours corresponding to the top panel model lines, with a horizontal line at 0 to guide the eye.

**Table 2.** MCMC results for WASP-94 A and the derived 3D spin-orbit obliquity using solid-body (SB) stellar rotation model with centre-to-limb convective variations (CLVs) or differential rotation (DR) model. CLV1, CLV2, and CLV3 correspond to centre-to-limb linear, quadratic and cubic, respectively. The BIC of each model was calculated using  $\chi^2$  and the respective degrees of freedom.

Model	No. of model parameters	$v_{\text{eq}}$ (km s <sup>-1</sup> )	$i_*$ (°)	$\alpha$	$\lambda$ (°)	$c_1$	$c_2$	$c_3$	BIC	$\chi^2$	$\psi$ (°)
SB	2	$5.45 \pm 0.45$	90.0	0.0	$123.0 \pm 3.0$	–	–	–	71.1	63.8	–
SB + CLV1	3	$5.94 \pm 0.60$	90.0	0.0	$120.2 \pm 3.3$	$-0.28 \pm 0.25$	–	–	73.2	62.4	–
SB + CLV2	4	$5.95 \pm 0.65$	90.0	0.0	$120.6 \pm 3.5$	$-0.48 \pm 2.0$	$0.1 \pm 1.3$	–	79.4	65.0	–
SB + CLV3	5	$7.07 \pm 0.80$	90.0	0.0	$114.8 \pm 3.2$	$-26.3 \pm 12$	$38 \pm 17$	$-17.8 \pm 8.0$	75.5	57.4	–
DR	4	$5.82 \pm 2$	$101.0^{+29}_{-53}$	$-0.07 \pm 0.25$	$126.2 \pm 5.0$	–	–	–	118	103	–

a differential rotation scenario to the local RVs, where the result can be seen in Table 2. In this case, we find a bimodal distribution to be present in  $i_*$ , which indicates a degeneracy, likely caused by the spectroscopic transits from HARPS and CORALIE not being precise enough to separate between the stars pointing away or towards us. We also ran the MCMC fitting for DR fixing  $i_* < 90^\circ$  (away) and  $i_* > 90^\circ$  (towards) to get an estimate on  $i_*$  and  $\alpha$ . Overall, we found these models had a higher BIC than the SB models, and  $\alpha$  was consistent with zero. Note that we ran additional DR models that include CLV variations and are not listed in Table 2 as they showed equivalent behaviour to the DR-only model.

In summary, we find the solid body, SB, rotation model is the best fit to the local RVs with a  $v_{\text{eq}} \sin i_* = 5.45 \pm 0.45$  km s<sup>-1</sup> (from

spectral line broadening in Neveu-Vanmalle et al. (2014)  $v_{\text{eq}} \sin i_* = 4.2 \pm 0.5$  km s<sup>-1</sup>, which agrees within  $2\sigma$ ) and refined projected obliquity of  $\lambda = 123.0 \pm 3.0^\circ$ . The projected obliquity lies within  $1.5\sigma$  and the  $v_{\text{eq}} \sin i_*$  lies within  $2.5\sigma$  of the values determined by Neveu-Vanmalle et al. (2014).

## 5 TRANSMISSION SPECTRUM

We follow Seidel et al. (2019) to calculate the transmission spectrum in the order of the Na doublet. We separate the planetary signal from the stellar signal by using the out-of-transit data to create a master spectrum of the star. The in-transit spectra are shifted by the various

Doppler shifts moving from the observer's rest frame to the planetary rest frame, in which the results are provided.

### 5.1 Telluric correction

The main impact on transmission spectroscopy from the ground is the absorption of light by Earth's atmosphere, which creates additional absorption lines in our spectra. Depending on the relative velocity between the observer and the planet, these lines can overlap with the stellar Na doublet and distort the amplitude and shape of the lines. The established tool to correct for this effect in the optical is MOLECFIT (Kausch et al. 2015; Smette et al. 2015), an ESO tool for correcting telluric absorption lines in ground-based high-resolution data (version 1.15.0). We applied the same parameters as used in Allart et al. (2017). For recent applications of MOLECFIT to the range of the Na doublet for HARPS data, see Hoeijmakers et al. (2020), Seidel et al. (2020), Mounzer et al. (2022); Steiner et al. (2023). For a more comprehensive overview of different methods to correct tellurics, see Langeveld et al. (2021), with the caveat that they employ an outdated version of MOLECFIT for their assessment. A visual inspection of the corrected versus uncorrected spectra showed no over- or under-correction of the telluric lines around the Na doublet. All telluric lines were reduced to the noise level.

A second source of telluric contamination is the emission of telluric Na. The Na layer in Earth's mesosphere can get excited by meteor showers, introducing Na emission features in the Na D doublet. Both the thickness of the layer and the occurrence of meteor showers depend on season and location and thus contamination is not easily predicted. To check for these emission features, fibre B of HARPS is set to the sky and measures the background. We did not find any contamination on fibre B for the presented data set.

### 5.2 Stellar correction

After the telluric correction was performed, each spectrum was shifted into the stellar rest frame by using the systemic velocity, the barycentric Earth radial velocity (BERV) and the stellar velocity. This was done so that the stellar proportion of each spectrum can be identified as it is constant in the stellar rest frame and eliminated, leaving solely the planet's spectral contribution.

We masked any flux measurements of  $<200$  electrons per pixel as data at this level is dominated by read-out noise instead of photon noise. These data thus introduce spurious contamination from the instrument and can potentially mask a planetary signal. A total of 44 pixels were masked, which is an average of 0.8 per exposure.

While the stellar spectrum does not vary in principle, centre-to-limb variations and the RM effect change our stellar spectra and affect the transmission spectrum. This is likely to be undetectable for slow-rotating stars, but might cause masking of features for stars with rotation (Wytttenbach et al. 2020). However, different correction methods are currently in use (e.g. Wytttenbach et al. 2020; Casasayas-Barris et al. 2021) and we, therefore, test two methods for correcting for these two effects. Note that WASP-94 A is also an F-type star where limb variations are not as pronounced as earlier type stars (e.g. see Csizmadia 2018).

#### 5.2.1 Numerical correction

First, we followed the stellar correction as described by Wytttenbach et al. (2020), which uses local stellar spectra (the stellar spectrum behind the planet during the transit) generated from the out-of-transit

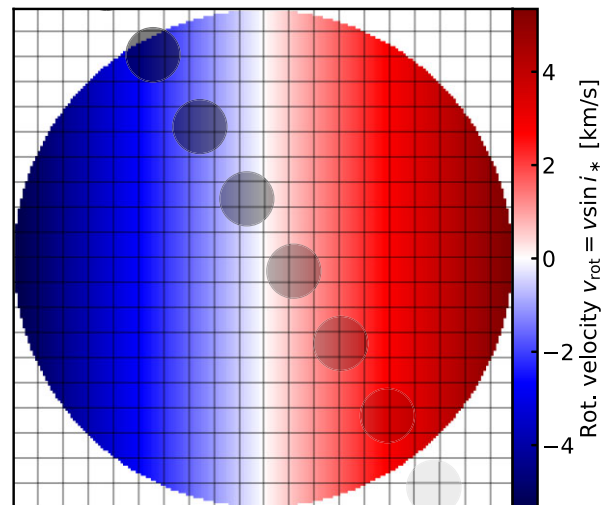


**Figure 3.** Illustration of the transit of WASP-94 A b, showing the position of the planet at every 4th exposure starting at the bottom right. As it is retrograde, it blocks the red-shifted region from the star during the first half of the transit and the blue-shifted area during the second half.

spectra and the transit depth of the planet to calculate the RM effect and limb-darkening variations for the observed transmission annulus.

For the transit depth and limb-darkening, we utilized the BATMAN PYTHON package (Kreidberg 2015) to compute the flux change due to WASP-94 A b at each point during the transit. For the local stellar spectra, we used the local RVs computed from RM effect analysis as described in Section 4 to create shifted stellar spectra (from the out-of-transit data) that represent the local stellar spectra at each point during the transit.

#### 5.2.2 Modelled correction

As an alternative and to ensure the accuracy of our RM and CLVs correction, we modelled the effect using the open-source STARROTATOR PYTHON package.<sup>1</sup> Using input star and planetary parameters, STARROTATOR generates the stellar spectrum during the transit. The stellar spectrum was calculated using the Vienna Atomic Line Database (VALD; Piskunov et al. 1995; Ryabchikova et al. 2015) in combination with the PYTHON installation of Spectroscopy Made Easy (SME; Valenti & Piskunov 1996; Piskunov & Valenti 2017; Wehrhahn, Piskunov & Ryabchikova 2023), which are commonly used for propagating RM and CLVs effects for high-resolution transmission spectroscopy (e.g. Casasayas-Barris et al. 2019; Yang et al. 2024).

The star input parameters were based on the preferred solid-body model following our RM analysis (see Table 2), and the planet parameters followed Table 1 except for the transit depth and limb-darkening parameters, which were taken from the light curve fit of WASP-94 A b's transit in the Na doublet in low spectral resolution (Ahrer et al. 2022). This code then allows us to calculate the RM effect at the spectral resolution of HARPS for the planet phases we observed, as illustrated in Fig. 3. We were able to utilize this to correct our in-transit stellar spectra by dividing out the modelled RM effect in each spectrum.

<sup>1</sup>Github: <https://github.com/Hoeijmakers/StarRotator>, accessed: 2023-12-07

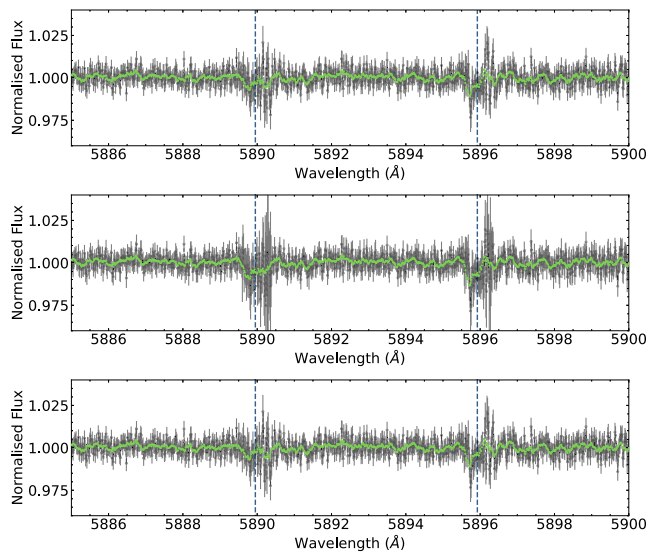


**Figure 4.** HARPS transmission spectrum of WASP-94 A b in the planetary rest frame, for the wavelength range with the Na doublet. The black points represent the data, while the green line shows the running median over 10 points. The two lines from the Na doublet,  $D_2$  and  $D_1$ , are indicated with the vertical dashed lines at 0.588995 and 0.589592  $\mu\text{m}$ , respectively. *Top panel:* Transmission spectrum without any corrections for the RM effect or centre-to-limb variations (CLVs). *Centre panel:* Transmission spectrum using the numerical RM and CLVs correction by Wyttenbach et al. (2020). *Bottom panel:* Transmission spectrum applying an RM and CLVs correction based on a generated model using STARROTATOR. Note that the correction is almost non-visible (compared to the top panel), with a maximum effect of 0.5 per cent at the beginning and the end of the transit, which is just about smaller than the average uncertainty.

## 5.3 Results

### 5.3.1 Transmission spectrum

The transmission spectrum was computed by moving each corrected in-transit spectrum into the planet's rest frame, using the planet's velocity at each point in time. These spectra were then summed and normalized by the mean value. We did not take into account any frames, where the planetary Na line falls onto the same wavelength bin as the stellar line to avoid any contamination from residuals of the stellar correction.

We computed the transmission spectrum for three cases, shown in Fig. 4: (1, top panel) without a correction for the RM effect and centre-to-limb variations, (2, middle panel) RM effect and CLVs is corrected for using the numerical method by Wyttenbach et al. (2020), see Section 5.2.1, and (3, bottom panel) using a STARROTATOR model to remove effects by the RM and CLVs, see Section 5.2.2.

As a result, in Fig. 4, we see that the Na doublet in the transmission spectrum of WASP-94 A b demonstrates an unusual W-shape using both the numerical and modelled correction for the RM and CLVs. Note that the transmission spectrum using the numerical correction (centre) shows higher uncertainties as we take the uncertainties in the local stellar spectra into account.

### 5.3.2 False-positive assessment

A wrongly identified – ‘false-positive’ – detection can occur due to systematic noise, e.g. from instrumental effects, stellar spots,

varying observing conditions, etc. The probability of such a false-positive detection can be estimated using a bootstrapping analysis with an Empirical Monte Carlo (EMC) introduced by Redfield et al. (2008).

For this purpose, we create two independent data sets from our data, where one includes the in-transit data while the other consists of the out-of-transit data, all in the planetary rest frame. Following Redfield et al. (2008), we randomly draw in-transit and out-of-transit data sets to create a virtual transmission spectrum. We consider three scenarios: (1) ‘in–in’, where all drawn spectra are taken from the real in-transit data and randomly considered either in- or out-of-transit for our virtual transmission spectrum; (2) ‘out–out’, where all spectra are drawn from the real out-of-transit data and randomly considered as either in- or out-of-transit for our virtual transmission spectrum; (3) ‘in–out’, where the virtual transmission spectrum is created using randomly drawn real in-transit and out-of-transit spectra for the virtual in- and out-of-transit spectra. In the case where the detection is not spurious and indeed of planetary nature, we expect that only the ‘in–out’ scenario shows a detection.

The results of this bootstrapping assessment are shown in Fig. 5, where we conducted this analysis using the in-transit spectra when correcting using the numerical correction (Section 5.2.1) and the STARROTATOR modelled correction (Section 5.2.2). Both of them show that ‘in–in’ and ‘out–out’ are centred at zero, while the ‘in–out’ is non-zero with a fitted peak at  $\approx -0.1$  per cent and a standard deviation of  $\approx 0.03$  per cent, thus ruling out a spurious detection of a planetary atmosphere due to systematic effects.

### 5.3.3 Na absorption depth

We fitted Gaussian profiles to both lines in the Na doublet of the two transmission spectra retrieved with the numerical and modelled stellar correction using a nested sampling algorithm (POLYCHORD; Handley, Hobson & Lasenby 2015). The resulting fits are shown in Fig. 6. The Gaussian fit to both lines is strongly favoured over a straight line with a Bayesian evidence difference of 9.5 ( $\approx 4.0\sigma$ ) and 8.5 ( $\approx 2.7\sigma$ ) for the numerical and modelled approach, respectively.

We calculated the relative absorption depth by averaging the flux in the Na lines and comparing it to the average flux in chosen reference bands in the continuum, following, e.g. Charbonneau et al. (2002). We selected a blue (B) and red (R) control wavelength band with a width of 12  $\text{\AA}$ , at 5874–5886  $\text{\AA}$  and 5898–5910  $\text{\AA}$ , respectively. The fluxes at the Na doublet are then summed within an area of 1.5, 3, 6, and 12  $\text{\AA}$  on each side of each line core (following, e.g. Wyttenbach et al. 2015, 2017; Seidel et al. 2019) and subtracted from the average of the fluxes in the B and R wavelength bands. The absorption depths found are displayed in Table 3 with their respective detection levels. For the two narrowest Na bands, the depths range from 0.118 per cent up to 0.209 per cent with detection significances of  $2.7\sigma$  up to  $4.4\sigma$ . This is also consistent with the significance found using the Bayesian evidence model differences between fitting a straight line and fitting Gaussian functions to the absorption lines discussed at the beginning of this section.

## 6 ATMOSPHERIC RETRIEVAL

We perform atmospheric retrievals with HyDRA-H (Gandhi et al. 2019, 2022), combining the high spectral resolution observations with HARPS using the numerical stellar correction (as it showed the larger Na feature and is based on our real data) with low resolution observations taken with the NTT (Ahrer et al. 2022). Our set up

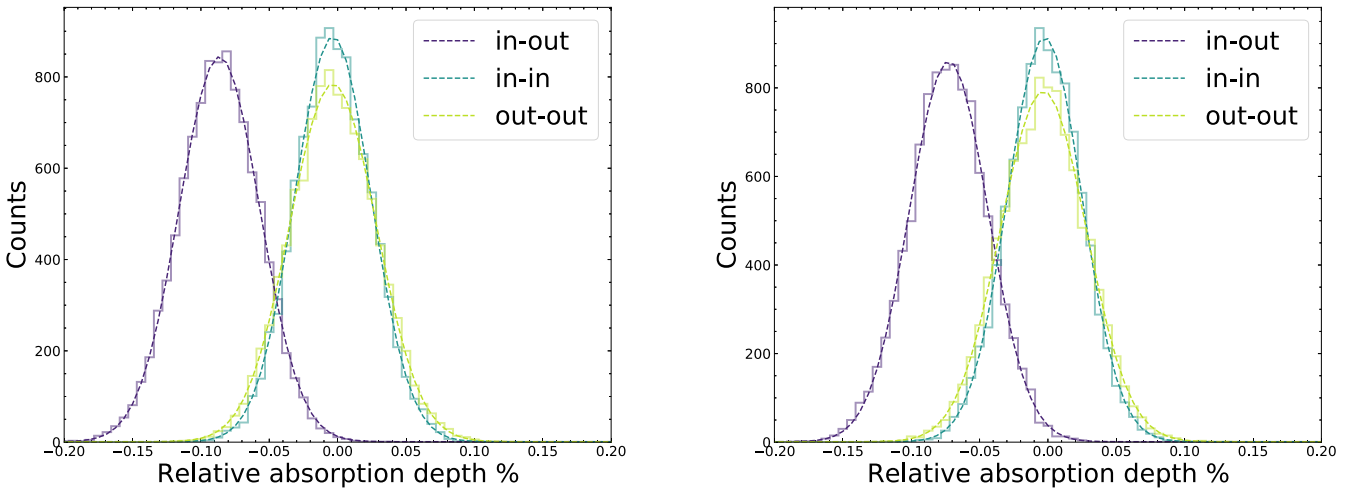


**Figure 5.** Distribution of our bootstrapping analysis for the Na doublet for 5000 random selections for the stellar-corrected spectra using the numerical RM correction (left) and using the STARROTATOR modelled correction (right). The ‘in–out’ describes the case where an in- and out-of-transit spectrum were used, while the ‘in–in’ and ‘out–out’ describe the cases where only in- and only out-of-transit spectra were utilized, respectively. Therefore, the ‘in–out’ distribution is the only one that is expected to be centred at a non-zero value if the signal is indeed of planetary origin, which is true in both cases, slightly stronger using the numerical RM correction (left).

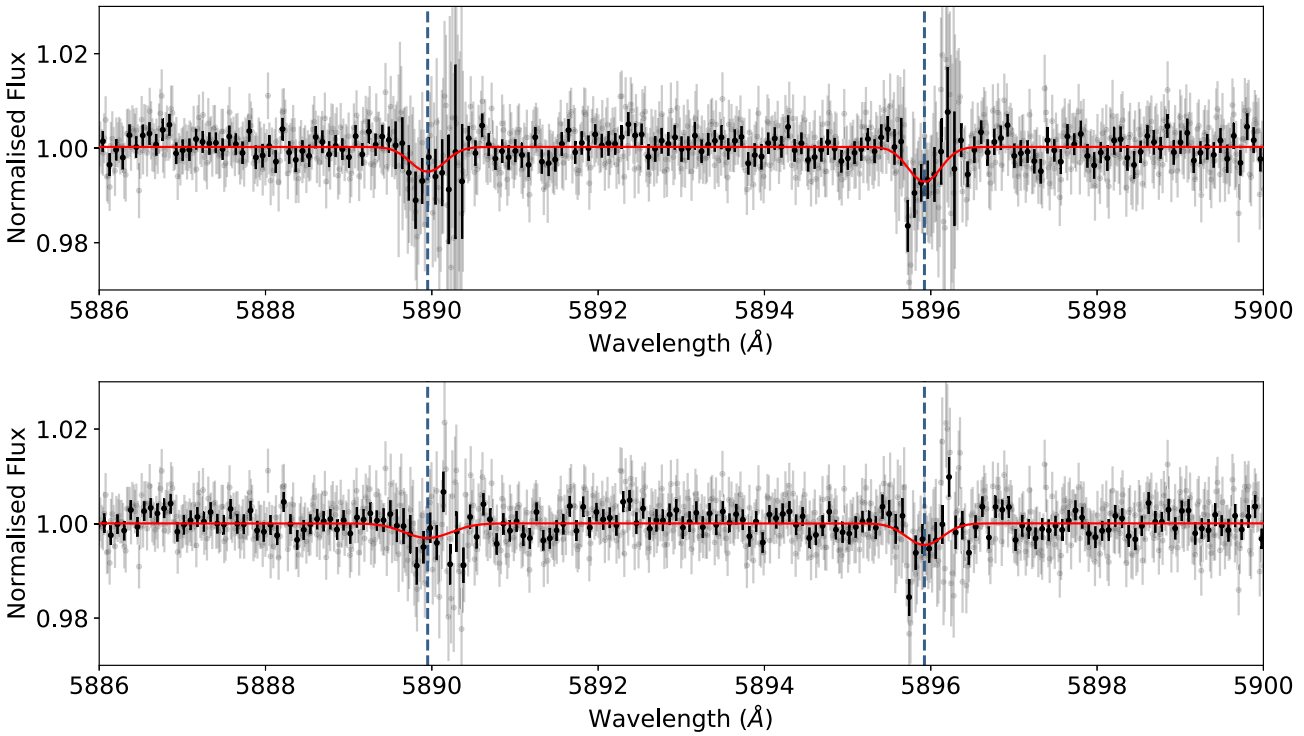


**Figure 6.** WASP-94 A b transmission spectrum binned in black and unbinned in light grey with a Gaussian fit to both Na doublet lines in red. *Top panel:* Transmission spectrum retrieved with numerical stellar correction method (Section 5.2.1) and its fitted Gaussian function. *Bottom panel:* Transmission spectrum retrieved with modelled stellar correction (Section 5.2.2) and its Gaussian fit.

includes three free parameters for the volume mixing ratios of H<sub>2</sub>O, Na, and K, with their opacities derived using the ExoMol line list for H<sub>2</sub>O (Polyansky et al. 2018), and the Kurucz line list for Na and K (Kurucz & Bell 1995). We additionally include six parameters that determine the temperature profile of the atmosphere using the method of Madhusudhan & Seager (2009). We also include a reference

pressure at which the planetary radius is set into our retrieval. We allow for partial clouds and hazes in the atmosphere of WASP-94 A b, using the cloud fraction as a free parameter (Line & Parmentier 2016). For the high-resolution observations, we also include two additional parameters, the deviation from the planet’s known systemic velocity,  $dV_{sys}$ , and a term to account for additional broadening introduced by

**Table 3.** Relative absorption depth and detection level of Na in the atmosphere of WASP-94 Ab (calculated as depth over the standard deviation), observed with HARPS for different wavelength band widths.

band	Numerical correction		Modelled correction	
	depth (per cent)	$\sigma$	depth (per cent)	$\sigma$
$2 \times 0.75 \text{ \AA}$	$0.209 \pm 0.058$	$3.7\sigma$	$0.149 \pm 0.055$	$2.7\sigma$
$2 \times 1.5 \text{ \AA}$	$0.147 \pm 0.034$	$4.4\sigma$	$0.118 \pm 0.033$	$3.6\sigma$
$2 \times 3 \text{ \AA}$	$0.062 \pm 0.023$	$2.8\sigma$	$0.047 \pm 0.022$	$2.2\sigma$
$2 \times 6 \text{ \AA}$	$0.040 \pm 0.018$	$2.3\sigma$	$0.028 \pm 0.017$	$1.7\sigma$

**Table 4.** Parameters and uniform prior ranges for our retrieval. We retrieve the Na, K, and H<sub>2</sub>O abundances, temperature profile, and partial cloud/haze parameters. Our temperature profile includes six free parameters, and our cloud/haze parametrization includes four free parameters (see Section 6). The quoted values retrieved values here are from using both high resolutions HARPS and low resolution NTT data.

Parameter	Prior range	Retrieval constraint
$\log(X_{\text{H}_2\text{O}})$	$\mathcal{U}(-15, -1)$	$-8.4^{+4.1}_{-4.0}$
$\log(X_{\text{Na}})$	$\mathcal{U}(-15, -1)$	$-6.6^{+1.6}_{-1.0}$
$\log(X_{\text{K}})$	$\mathcal{U}(-15, -1)$	$-6.7^{+2.0}_{-4.9}$
$T_{\text{top}}/\text{K}$	$\mathcal{U}(750, 3000)$	$1900^{+680}_{-1270}$
$\alpha_1 / \text{K}^{-\frac{1}{2}}$	$\mathcal{U}(0, 1)$	$0.7 \pm 0.2$
$\alpha_2 / \text{K}^{-\frac{1}{2}}$	$\mathcal{U}(0, 1)$	$0.6^{+0.3}_{-0.2}$
$\log(P_1/\text{bar})$	$\mathcal{U}(-6, 2)$	$-1.6 \pm 1.6$
$\log(P_2/\text{bar})$	$\mathcal{U}(-6, 2)$	$-4.1^{+1.6}_{-1.2}$
$\log(P_3/\text{bar})$	$\mathcal{U}(-2, 2)$	$0.6^{+0.9}_{-1.2}$
$\log(P_{\text{ref}}/\text{bar})$	$\mathcal{U}(-4, 2)$	$-3.4^{+0.7}_{-0.9}$
$\log(\alpha_{\text{haze}})$	$\mathcal{U}(-4, 6)$	$1.7^{+2.1}_{-3.3}$
$\gamma_{\text{haze}}$	$\mathcal{U}(-20, -1)$	$-12.3^{+6.3}_{-5.0}$
$\log(P_{\text{cl}}/\text{bar})$	$\mathcal{U}(-6, 2)$	$-3.2^{+1.4}_{-1.2}$
$\phi_{\text{cl}}$	$\mathcal{U}(0, 1)$	$0.7^{+0.2}_{-0.3}$
$dV_{\text{sys}}$	$\mathcal{U}(-50, 50)$	$-2.1^{+6.2}_{-5.4}$
Rotation rate/km s <sup>-1</sup>	$\mathcal{U}(0, 50)$	$12.2^{+11.2}_{-5.7}$

the rotation velocity of the planet. Overall, our retrieval has 16 free parameters, with the prior ranges shown in Table 4.

We perform three retrievals, one using both data sets as well as one for each data set individually. The retrieved parameters using both low- and high-resolution data are shown next to their priors in Table 4. The low-resolution NTT/EFOSC2 data is shown in Fig. 7 along with the combined and individual retrieved model.

While most parameters were consistent across all retrievals, the abundance of Na and cloud-top level show tighter constraints when combining the low- and high spectral resolution from NTT and HARPS, as seen in Fig. 8. However, when computing the detection significance for Na by comparing the Bayesian evidence for models with and without Na, we did not find a significant improvement when retrieving Na on both low- and high-resolution data sets with  $2.6\sigma$  (NTT only),  $3.1\sigma$  (HARPS only), and  $3.2\sigma$  (NTT + HARPS combined).

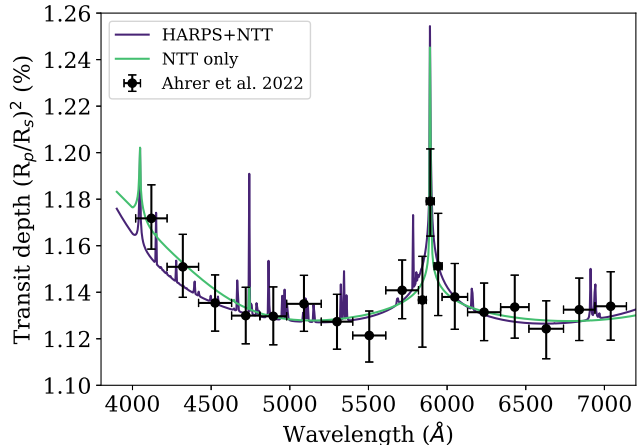


**Figure 7.** Low spectral resolution transmission spectrum of WASP-94 Ab using NTT/EFOSC2 (black) as published by Ahrer et al. (2022) with our retrieved models using NTT data only (NTT only, turquoise) and combining it with our HARPS observations (HARPS + NTT, dark blue).

## 7 DISCUSSION AND CONCLUSIONS

### 7.1 Orbital misalignment

With our analysis of the RM effect, we have confirmed the previously suggested retrograde orbit of WASP-94 Ab (Neveu-Vanmalle et al. 2014) and retrieved constraints on the projected spin-orbit obliquity of  $\lambda = 123 \pm 3^\circ$ . The orbital misalignment of WASP-94 Ab allows us to draw some conclusions about the system's formation and evolution.

Its close-in orbit makes it unlikely that WASP-94 Ab formed around the stellar companion, WASP-94 B, and was dynamically exchanged between the two stars (Moeckel & Veras 2012), or that its highly inclined orbit could be explained by capture of a free-floating planet in analogy to the retrograde orbit of Neptune's moon Triton (Agnor & Hamilton 2006; Goulianski & Ribak 2018).

Therefore, WASP-94 Ab likely formed in situ around WASP-94 A and then migrated to its current orbital configuration. Models in which planets migrate within the protoplanetary disc achieve lower obliquities than that required here (Lin & Papaloizou 1986; Millholland & Spalding 2020), suggesting that WASP-94 Ab migrated after its protoplanetary disc had dissipated. Similarly, perturbations driven by planetary mass companions also struggle to achieve high obliquities (Chatterjee et al. 2008; Petrovich & Tremaine 2016).

The stellar companion WASP-94 B is then likely the origin of the perturbation that drove WASP-94 Ab towards its current orbit (see fig. 24 of Albrecht, Dawson & Winn 2022 for a comparison of the obliquity distributions produced by various misalignment mechanisms). The well-studied Kozai-Lidov mechanism (Kozai 1962; Lidov 1962) involves a distant companion driving alternating cycles of high eccentricity and inclination for an inner companion and has been widely invoked to form hot Jupiters (e.g. Holman, Touma & Tremaine 1997; Wu & Murray 2003; Naoz et al. 2011). Kozai-Lidov cycles driven by a stellar companion can force planets onto high obliquity and even retrograde orbits (Naoz et al. 2011; Li et al. 2014; Anderson, Storch & Lai 2016). The planet's pericentre can be driven to small enough distances that tidal interactions between the planet and star can disrupt the cycle and cause the planet's orbit to shrink and circularize at its frozen in orientation (e.g. Rasio &

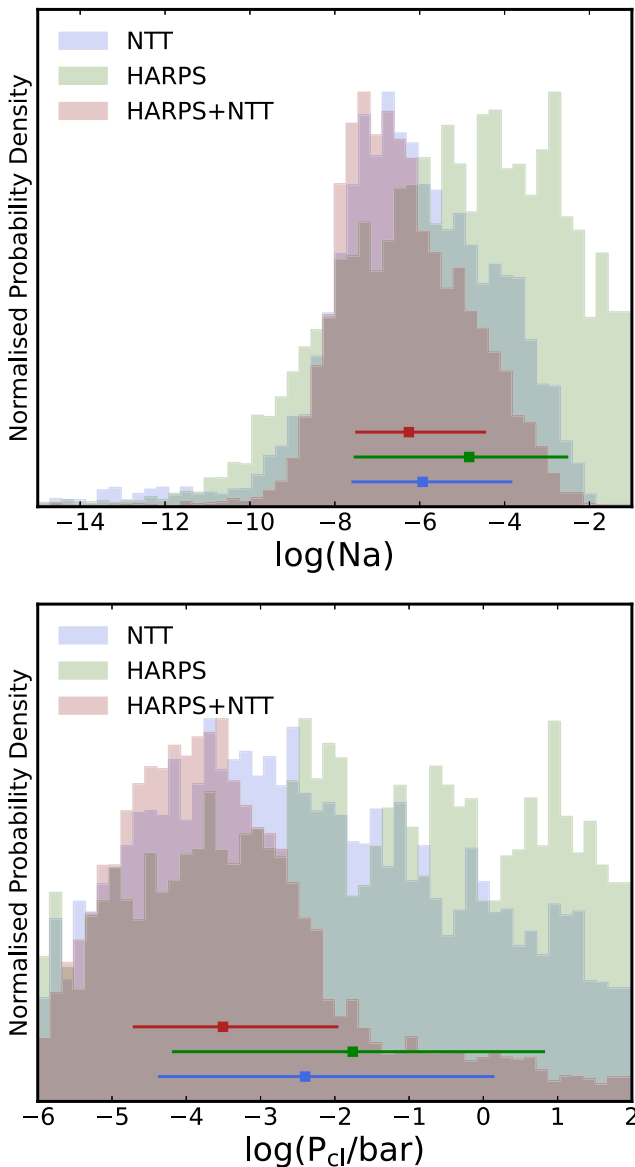


**Figure 8.** Posterior distributions of the atmospheric retrieval analysis using the HARPS observations from this work, applying a numerical correction to the RM-effect, which showed higher detection significance than the modelled approach (see Section 5.3.3 and Table 3) and combined with the low spectral resolution data (NTT) from Ahrer et al. (2022). *Top panel:* Constraints on the abundance of Na from NTT, HARPS, and combined. *Bottom panel:* Constraints on the cloud-top level from NTT, HARPS, and combined.

Ford 1996; Fabrycky & Tremaine 2007; Matsumura, Peale & Rasio 2010), producing a misaligned hot Jupiter.

The effective temperature of WASP-94 A ( $T_{\text{eff}} = 6194 \pm 5$  K, Teske et al. 2016) places it close to the Kraft break, which is a transition between fast-rotating hot stars and cooler stars with thicker convective envelopes and slower rotations due to magnetic braking (Kraft 1967; Dawson 2014; Albrecht et al. 2022). Previous studies have identified that stars above  $T_{\text{eff}} = 6000$  K host hot Jupiters with a wider range of obliquities than cooler stars (Schlaufman 2010; Winn et al. 2010). This dichotomy has been attributed to changes in the tidal realignment time-scales driven by the different stellar structures on either side of the Kraft break (e.g. Albrecht et al. 2012).

Given WASP-94 A's effective temperature and metallicity (see Table 1), the Kraft break should be around  $\sim 6000$  K, placing WASP-94 A in the hot, fast rotating regime. Thus, WASP-94 A b is consistent with the previously identified pattern of highly oblique planets being hosted by hot ( $T_{\text{eff}} > 6000$  K) stars.

The full evolutionary history of the WASP-94 system required to produce the observed orbital configuration will be studied further in future work with the goal of placing additional constraints on the system parameters.

## 7.2 Transmission spectrum

Using observations of one transit with HARPS, we find tentative evidence for Na in the atmosphere of WASP-94 A b. Depending on the treatment of the RM correction, we find detection significances of  $3.7\text{--}4.4\sigma$  and  $2.7\text{--}3.6\sigma$ .

While we used state-of-the-art methods to correct for telluric and stellar effects, we still found unusual structures in the transmission spectrum instead of Gaussian-shaped Na doublet absorption lines. For this reason, we investigated whether varying planet and stellar parameters within their  $1\sigma$  uncertainties could account for the observed shape, e.g. velocities computed by our RM analysis, systemic velocity, etc. However, we did not find any evidence for any planet or stellar parameters to alter the shape of the transmission significantly enough to explain the W-shape. Therefore, we conclude that the cloudy observing conditions and low flux in several frames are driving the noise structure in the transmission spectrum.

## 7.3 Atmospheric inferences combining with low resolution data

We combined our high-spectral resolution HARPS observations of the atmosphere of WASP-94 A b with low-resolution data from the literature (Ahrer et al. 2022) to test whether we can achieve tighter constraints and a higher detection significance when running an atmospheric retrieval analysis on both simultaneously.

We find that the abundance of Na and the cloud-top level did show tighter posterior distributions than each data set individually (see Fig. 8). However, the detection significance of Na performed by Bayesian model comparison against a retrieval without Na did not improve significantly. With our combined analysis, we find a significance of  $3.2\sigma$ , while the retrievals on the individual data sets result in  $2.6\sigma$  and  $3.1\sigma$  for NTT and HARPS, respectively. This only marginal increase in the detection of Na may be due to temperature degeneracies in the two data sets. While the low-resolution-only retrieval prefers a lower temperature, the high resolution one converges to a higher temperature. Consequently, the combined retrieval shows something in between, as shown in Table 4, more akin to the equilibrium temperature of the planet, thereby not increasing the overall detection significance of Na given the slight tension between the data sets. The fact the temperature is degenerate with the relative optical depth of Na was also found by Pino et al. (2018) in their study combining low- and high-resolution observations of hot Jupiter HD 189733b.

Nevertheless, these Na detection significances comply with the ones found using solely the HARPS spectrum and comparing the Na doublet to surrounding bands as discussed in the previous section (see also Section 5.3.3), validating our sodium detection.

## 7.4 Future avenues

Further transit observations are needed to fully characterize the shape and potential offset of the Na absorption feature in the atmosphere

of this planet. WASP-94 Ab is an ESPRESSO GTO target, so we expect that the high-resolution signals from the planet's atmosphere will be further explored by this team in the near future.

In addition, WASP-94 Ab is scheduled to be observed by *JWST* in June 2024 (ID #3154; Ahrer et al. 2023b) to test C/O and metallicity predictions based on planet formation and migration models following its retrograde and misaligned orbit (e.g. Öberg, Murray-Clay & Bergin 2011; Madhusudhan, Amin & Kennedy 2014; Booth et al. 2017).

## ACKNOWLEDGEMENTS

EA acknowledges the financial support of the Department of Physics at the University of Warwick and the Max Planck Society. This work was supported by a UKRI Future Leaders Fellowship MR/T040866/1. RN acknowledges support from UKRI/EPSRC through a Stephen Hawking Fellowship (EP/T017287/1). CHM gratefully acknowledges support from the Leverhulme Centre for Life in the Universe at the University of Cambridge. PJW acknowledges support from the Science and Technology Facilities Council (STFC) under consolidated grants ST/T000406/1 and ST/X001121/1. This work has made use of data from the European Space Agency (ESA) mission *Gaia* (<https://www.cosmos.esa.int/gaia>), processed by the *Gaia* Data Processing and Analysis Consortium (DPAC; <https://www.cosmos.esa.int/web/gaia/dpac/consortium>). This work has made use of the VALD data base, operated at Uppsala University, the Institute of Astronomy RAS in Moscow, and the University of Vienna.

## DATA AVAILABILITY

The raw and HARPS-pipeline processed data is available via the ESO archive, programme 097.C-1025(B), PI: Ehrenreich.

## REFERENCES

- Agnor C. B., Hamilton D. P., 2006, *Nature*, 441, 192
- Ahrer E., Wheatley P. J., Kirk J., Gandhi S., King G. W., Louden T., 2022, *MNRAS*, 510, 4857
- Ahrer E., Wheatley P. J., Gandhi S., Kirk J., King G. W., Louden T., Welbanks L., 2023a, *MNRAS*, 521, 5636
- Ahrer E.-M. et al., 2023b, Testing the C/O Ratio Prediction for Hot Jupiters from Disk-Free Migration, *JWST* Proposal. Cycle 2, ID. #3154
- Ahrer E. M. et al., 2023c, *Nature*, 614, 653
- Albrecht S. et al., 2012, *ApJ*, 757, 18
- Albrecht S. H., Dawson R. I., Winn J. N., 2022, *PASP*, 134, 082001
- Alderson L. et al., 2020, *MNRAS*, 497, 5182
- Alderson L. et al., 2023, *Nature*, 614, 664
- Allart R., Lovis C., Pino L., Wyttenbach A., Ehrenreich D., Pepe F., 2017, *A&A*, 606, A144
- Allart R. et al., 2019, *A & A*, 623, A58
- Anderson K. R., Storch N. I., Lai D., 2016, *MNRAS*, 456, 3671
- Andrae R. et al., 2023, *A&A*, 674, A27
- Bailer-Jones C. A. L., Rybizki J., Fouesneau M., Mantelet G., Andrae R., 2018, *AJ*, 156, 58
- Baranne A. et al., 1996, *A&AS*, 119, 373
- Bonfils X. et al., 2013, *A&A*, 549, A109
- Bonomo A. S. et al., 2017, *A&A*, 602, 107
- Booth R. A., Clarke C. J., Madhusudhan N., Ille J. D., 2017, *MNRAS*, 469, 3994
- Brogi M., Line M., Bean J., Désert J. M., Schwarz H., 2017, *ApJ*, 839, L2
- Carone L. et al., 2021, *A&A*, 646, A168
- Casasayas-Barris N. et al., 2018, *A&A*, 616, A151
- Casasayas-Barris N. et al., 2019, *A&A*, 628, A9
- Casasayas-Barris N. et al., 2021, *A&A*, 647, A26
- Cegla H. M., Lovis C., Bourrier V., Beeck B., Watson C. A., Pepe F., 2016, *A&A*, 588, A127
- Charbonneau D., Brown T. M., Latham D. W., Mayor M., 2000, *ApJ*, 529, L45
- Charbonneau D., Brown T. M., Noyes R. W., Gilliland R. L., 2002, *ApJ*, 568, 377
- Chatterjee S., Ford E. B., Matsumura S., Rasio F. A., 2008, *ApJ*, 686, 580
- Csizmadia S., 2018, Stellar Limb Darkening's Effects on Exoplanet Characterization. Springer International Publishing, Cham, Switzerland, p. 1403
- Dawson R. I., 2014, *ApJ*, 790, L31
- Delisle J. B. et al., 2018, *A&A*, 614, A133
- Doyle L. et al., 2022, *MNRAS*, 516, 298
- Dyrek A. et al., 2024, *Nature*, 625, 51
- Ehrenreich D. et al., 2020, *Nature*, 580, 597
- Espinosa N. et al., 2019, *MNRAS*, 482, 2065
- Fabrycky D., Tremaine S., 2007, *ApJ*, 669, 1298
- Feinstein A. D. et al., 2023, *Nature*, 614, 670
- Foreman-Mackey D., Hogg D. W., Lang D., Goodman J., 2013, *PASP*, 125, 306
- Gaia Collaboration et al., 2023, *A&A*, 674, A1
- Gandhi S., Madhusudhan N., Hawker G., Piette A., 2019, *AJ*, 158, 228
- Gandhi S., Kesseli A., Snellen I., Brogi M., Wardenier J. P., Parmentier V., Welbanks L., Savel A. B., 2022, *MNRAS*, 515, 749
- Garhart E. et al., 2020, *AJ*, 159, 137
- Gouliinski N., Ribak E. N., 2018, *MNRAS*, 473, 1589
- Handley W. J., Hobson M. P., Lasenby A. N., 2015, *MNRAS*, 453, 4384
- Hoeijmakers H. J. et al., 2018, *Nature*, 560, 453
- Hoeijmakers H. J. et al., 2019, *A&A*, 627, A165
- Hoeijmakers H. J. et al., 2020, *A&A*, 641, A123
- Holman M., Touma J., Tremaine S., 1997, *Nature*, 386, 254
- Huitson C. M. et al., 2013, *MNRAS*, 434, 3252
- Kausch W. et al., 2015, *A&A*, 576, A78
- Khalafinejad S. et al., 2021, *A&A*, 656, A142
- Kirk J., Wheatley P. J., Louden T., Doyle A. P., Skillen I., McCormac J., Irwin P. G. J., Karjalainen R., 2017, *MNRAS*, 468, 3907
- Kozai Y., 1962, *AJ*, 67, 591
- Kraft R. P., 1967, *ApJ*, 150, 551
- Kreidberg L., 2015, *PASP*, 127, 1161
- Kreidberg L. et al., 2014, *Nature*, 505, 69
- Kreidberg L., Line M. R., Thorngren D., Morley C. V., Stevenson K. B., 2018, *ApJ*, 858, L6
- Kurucz R. L., Bell B., 1995, Atomic Line Data. Smithsonian Astrophysical Observatory, Cambridge, MA
- Langeveld A. B., Madhusudhan N., Cabot S. H. C., Hodgkin S. T., 2021, *MNRAS*, 502, 4392
- Lecavelier Des Etangs A., Pont F., Vidal-Madjar A., Sing D., 2008, *A&A*, 481, 83
- Li G., Naoz S., Kocsis B., Loeb A., 2014, *ApJ*, 785, 116
- Lidov M. L., 1962, *Planet. Space Sci.*, 9, 719
- Lin D. N. C., Papaloizou J., 1986, *ApJ*, 309, 846
- Line M. R., Parmentier V., 2016, *ApJ*, 820, 78
- Madhusudhan N., Seager S., 2009, *ApJ*, 707, 24
- Madhusudhan N., Amin M. A., Kennedy G. M., 2014, *ApJL*, 794, 12
- Matsumura S., Peale S. J., Rasio F. A., 2010, *ApJ*, 725, 1995
- Mayor M., Queloz D., 1995, *Nature*, 378, 355
- Mayor M. et al., 2003, *The Messenger*, 114, 20
- McLaughlin D. B., 1924, *ApJ*, 60, 22
- Millholland S. C., Spalding C., 2020, *ApJ*, 905, 71
- Moeckel N., Veras D., 2012, *MNRAS*, 422, 831
- Mounzer D. et al., 2022, *A&A*, 668, A1
- Naoz S., Farr W. M., Lithwick Y., Rasio F. A., Teyssandier J., 2011, *Nature*, 473, 187
- Neveu-Vanmalle M. et al., 2014, *A&A*, 572, A49
- Nikolov N. et al., 2018, *Nature*, 557, 526
- Öberg K. I., Murray-Clay R., Bergin E. A., 2011, *ApJ*, 743, 16
- Petrovich C., Tremaine S., 2016, *ApJ*, 829, 132
- Pino L. et al., 2018, *A&A*, 612, A53

- Piskunov N., Valenti J. A., 2017, *A&A*, 597, A16
- Piskunov N. E., Kupka F., Ryabchikova T. A., Weiss W. W., Jeffery C. S., 1995, *A&AS*, 112, 525
- Polyansky O. L., Kyuberis A. A., Zobov N. F., Tennyson J., Yurchenko S. N., Lodi L., 2018, *MNRAS*, 480, 2597
- Pont F., Sing D. K., Gibson N. P., Aigrain S., Henry G., Husnoo N., 2013, *MNRAS*, 432, 2917
- Prineth B. et al., 2022, *Nat. Astron.*, 6, 449
- Queloz D., Eggenberger A., Mayor M., Perrier C., Beuzit J. L., Naef D., Sivan J. P., Udry S., 2000, *A&A*, 359, L13
- Rasio F. A., Ford E. B., 1996, *Science*, 274, 954
- Redfield S., Endl M., Cochran W. D., Koesterke L., 2008, *ApJ*, 673, L87
- Rossiter R. A., 1924, *ApJ*, 60, 15
- Rustamkulov Z. et al., 2023, *Nature*, 614, 659
- Ryabchikova T., Piskunov N., Kurucz R. L., Stempels H. C., Heiter U., Pakhomov Y., Barklem P. S., 2015, *Phys. Scr.*, 90, 054005
- Salz M. et al., 2018, *A&A*, 620, A97
- Schlaufman K. C., 2010, *ApJ*, 719, 602
- Seager S., Sasselov D. D., 2000, *ApJ*, 537, 916
- Seidel J. V. et al., 2019, *A&A*, 623, A166
- Seidel J. V. et al., 2020, *A&A*, 641, L7
- Sing D. K. et al., 2015, *MNRAS*, 446, 2428
- Sing D. K. et al., 2016, *Nature*, 529, 59
- Smette A. et al., 2015, *A&A*, 576, A77
- Snellen I. A., Albrecht S., De Mooij E. J., Le Poole R. S., 2008, *A&A*, 487, 357
- Snellen I. A., De Kok R. J., De Mooij E. J., Albrecht S., 2010, *Nature*, 465, 1049
- Spake J. J. et al., 2018, *Nature*, 557, 68
- Spryatos P. et al., 2021, *MNRAS*, 506, 2853
- Steiner M. et al., 2023, *A&A*, 672, A134
- Taylor J. et al., 2023, *MNRAS*, 524, 817
- Teske J. K., Khanal S., Ramírez I., 2016, *ApJ*, 819, 19
- The JWST Transiting Exoplanet Community Early Release Science Team et al., 2023, *Nature*, 614, 649
- Udry S. et al., 2007, *A&A*, 469, L43
- Unger N. et al., 2021, *A&A*, 654, A104
- Valenti J. A., Piskunov N., 1996, *A&AS*, 118, 595
- Wakeford H. R., Sing D. K., 2015, *A&A*, 573, A122
- Wehrhahn A., Piskunov N., Ryabchikova T., 2023, *A&A*, 671, A171
- Winn J. N., Fabrycky D., Albrecht S., Johnson J. A., 2010, *ApJ*, 718, L145
- Wu Y., Murray N., 2003, *ApJ*, 589, 605
- Wyttenbach A., Ehrenreich D., Lovis C., Udry S., Pepe F., 2015, *A&A*, 577, A62
- Wyttenbach A. et al., 2017, *A&A*, 602, A36
- Wyttenbach A. et al., 2020, *A&A*, 638, 87
- Yang Y., Chen G., Wang S., Yan F., 2024, *AJ*, 167, 36

This paper has been typeset from a TeX/LaTeX file prepared by the author.